Article

Optical Absorption in Tilted Geometries as an Indirect Measurement of Longitudinal Plasma Waves in Layered Cuprates

Niccolò Sellati [ID], Jacopo Fiore [ID], Claudio Castellani [ID] and Lara Benfatto *[ID]

Department of Physics and ISC-CNR, "Sapienza" University of Rome, P.le Aldo Moro 5, 00185 Rome, Italy; niccolo.sellati@uniroma1.it (N.S.); jacopo.fiore@uniroma1.it (J.F.); claudio.castellani@roma1.infn.it (C.C.)

* Correspondence: lara.benfatto@roma1.infn.it

Abstract: Electromagnetic waves propagating in a layered superconductor with arbitrary momentum, with respect to the main crystallographic directions, exhibit an unavoidable mixing between longitudinal and transverse degrees of freedom. Here we show that this basic physical mechanism explains the emergence of a well-defined absorption peak in the in-plane optical conductivity when light propagates at small tilting angles relative to the stacking direction in layered cuprates. More specifically, we show that this peak, often interpreted as a spurious leakage of the c-axis Josephson plasmon, is instead a signature of the true longitudinal plasma mode occurring at larger momenta. By combining a classical approach based on Maxwell's equations with a full quantum derivation of the plasma modes based on modeling the superconducting phase degrees of freedom, we provide an analytical expression for the absorption peak as a function of the tilting angle and light polarization. We suggest that an all-optical measurement in tilted geometry can be used as an alternative way to access plasma-wave dispersion, usually measured by means of large-momenta scattering techniques like resonant inelastic X-ray scattering (RIXS) or electron energy loss spectroscopy (EELS).

Keywords: layered superconductors; far-infrared conductivity; anisotropic response; Josephson plasmons; dielectric tensor

1. Introduction

In superconductors, the breaking of the continuous gauge symmetry below the superconducting (SC) critical temperature is accompanied by the emergence of two collective modes, associated with the amplitude (Higgs) or phase (Goldstone) fluctuation of the complex SC order parameter, whose absolute value at equilibrium defines the spectral gap for single-particle excitations [1]. While the former is a massive excitation, the latter is massless at a long wavelength, reflecting the infinity of possible ground states connected by a global change of the order-parameter phase. Nonetheless, the coupling of the SC phase to the electron density is directly affected by long-range Coulomb interactions between charged electrons. This effect moves the phase mode to the plasma energy scale [2], which is usually much larger than the spectral gap. As a consequence, optical signatures at the plasma energy scale, i.e., at the zero of the dielectric function, are usually unaffected by the SC transition. A rather different phenomenology is instead observed in anisotropically layered superconductors, i.e., systems where the pairing mainly occurs within planes stacked along the c direction, and the SC order is established below T_c thanks to a weak Josephson-like inter-plane interaction. The hallmark of this category is represented by high-temperature cuprates [3], where the marked anisotropy has been experimentally proven by different optical probes, starting from linear optics, which measures two well-separated energy scales for the plasma modes at long wavelengths for electric fields propagating in the CuO_2 planes or perpendicular to them. In these systems, the incoherent quasiparticle hopping along the stacking direction makes the c-axis response badly metallic: in contrast, below T_c, the opening of a sizable spectral gap along with the weak inter-layer pair hopping leaves a

rather sharp SC plasma edge at a frequency ω_c of a few THz in the optical reflectivity, which clearly testifies to the emergence of a well-defined SC Josephson plasmon. Even though this feature has been experimentally observed already in the late 1990s [4–9], renewed interest in the physics of Josephson plasmons has recently emerged. Such interest has been triggered both by the applications to nano-plasmonic [10,11] and by the role played by Josephson plasmons in non-linear THz spectroscopy[12–17]. In both cases, it becomes theoretically relevant to understand the momentum dependence of the plasmon dispersion at generic momentum, i.e., not along the main crystallographic axes. In this configuration, one immediately realizes that the anisotropy leads to a non-trivial response of the system, due to the fact that the current induced by the external electric field is no longer parallel to the field itself. As extensively discussed in Refs. [18–20], this mechanism leads to a mixing of the longitudinal and transverse responses inside the material, making the distinction between plasmons and polaritons blurred at momenta smaller than a scale $\bar{k} \sim \sqrt{\omega_{ab}^2 - \omega_c^2}/c$ set by the anisotropy between in-plane ω_{ab} and out-of-plane ω_c plasma frequencies. Since usually $\omega_{ab} \gg \omega_c$, the effect is relevant for non-linear Josephson plasmonics in the THz regime [21–24], but does not affect, e.g., the measurements of plasmons in RIXS [25–29] or EELS [30–32], which usually measure momenta in a fraction of the Brillouin zone. In the present manuscript, we investigate an additional consequence of the above-mentioned mixing, showing how even linear optics can be used to disentangle the longitudinal-transverse mixing in a reflection or transmission geometry, which highlights the emergence inside the material of a longitudinal response induced by an external transverse electromagnetic wave. The effect manifests as an absorption peak at a scale near ω_c for an electromagnetic wave traveling at a small angle with respect to the c direction. This feature has been measured in the past in different samples of electron-doped cuprates [33–36] below T_c, and it has often been interpreted as a leakage of the c-axis plasmon into the in-plane response [37]. Even more interestingly, the peak position has been shown to change by varying the wave polarization in the plane of incidence, considerably challenging the interpretation of the results. Here, we provide a full theoretical description of the microscopic mechanism behind the anomalous absorption peak, and we show that it is a direct consequence of the plasmon–polariton mixing in an anisotropically layered superconductor. We argue that this effect can be used to indirectly probe the plasmon dispersion that usually appears in RIXS and EELS experiments at much larger momenta and, by changing the light polarization, to extract the in-plane and out-of-plane plasma frequencies. Our findings are benchmarked against existing experimental data for cuprates. On a more general ground, our results offer a novel perspective on the possibility of accessing collective polariton modes in complex materials by properly engineering optical measurements.

2. Materials and Methods

We compute the optical conductivity for an anisotropic uniaxially layered superconductor as a response to an external electromagnetic wave traveling at a finite angle with respect to the stacking direction. We first address the problem within the standard approach of Maxwell's equations, leading to a general expression of the response at the finite angle as a function of the conductivity tensor along the main axes. To interpret the results in the case of a layered superconductor, and to make a connection with the generalized plasma modes discussed in Refs. [18–20], we address the same problem within a full-quantum path-integral formalism. In superconductors, plasma modes can be studied via the fluctuations θ of the phase of the SC order parameter. By coupling the electromagnetic field $\mathbf{A}$ to the SC phase via the minimal-coupling substitution $\boldsymbol{\nabla}\theta \to \boldsymbol{\nabla}\theta + 2e\mathbf{A}/c$, we can take into account electromagnetic interactions by properly including retardation effects, responsible for the longitudinal/transverse mixing at low momenta. By introducing appropriate gauge-invariant fields $\boldsymbol{\psi} = \boldsymbol{\nabla}\theta + 2e\mathbf{A}/c$ and after integrating out the matter degrees of freedom represented by θ, we obtain directly the transverse dielectric tensor, which assumes a simple expression in terms of the plasma modes of the systems and their large-momentum limit. Finally, we discuss the experimental configuration that makes it possible to measure the

plasma-mode dispersion and the in-plane and out-of-plane plasma frequencies by changing the light polarization. By computing the Fresnel conditions in the case of samples grown at a tilted angle, we demonstrate that our analytical results provide a quantitative estimate of the measured response. Conversely, the effect does not appear for non-tilted samples when the wave vector comes with a finite angle with respect to the stacking direction.

3. Results

3.1. Anisotropic Linear Response of Layered System

As discussed in the introduction, several experiments in electron-doped cuprates [33–36] have shown the emergence of a peak in the in-plane conductivity below T_c at a frequency close to that of the out-of-plane plasma edge, with the position shifting when the light polarization is changed. This peak is often interpreted as a spurious effect due to the leakage of the *c*-axis plasmon into the in-plane response [37], and light polarization is used to remove the effect [36]. However, in Ref. [35], the problem was investigated in detail by intentionally growing a sample with the stacking direction tilted with respect to the light wave vector, and a preliminary interpretation related to such a tilted geometry has been provided. Here, we will follow the same reasoning and study the response for a propagating wave vector at a tilted angle with respect to the stacking direction. To fix the notation, in the following, we will use the convention where the SC sheets are parallel to the *ab*-plane and stacked along the *c*-axis. We then assume, without loss of generality, that the momentum **k** of the propagating wave is along the *ac*-plane ($k_b = 0$). The angle between **k** and the *c*-axis is denoted as η and the angle between the transverse current and the *b*-axis is denoted as ϕ_J (see Figure 1 for the notation followed in this manuscript). Although discussing the Fresnel conditions at the sample/air boundary in such tilted geometries is not straightforward, we will postpone this analysis to the last section, and we will focus here on the behavior inside the sample. We are interested in determining the measured conductivity, defined as the ratio between the current **J** induced in the field direction and the modulus of the electric field **E** itself.
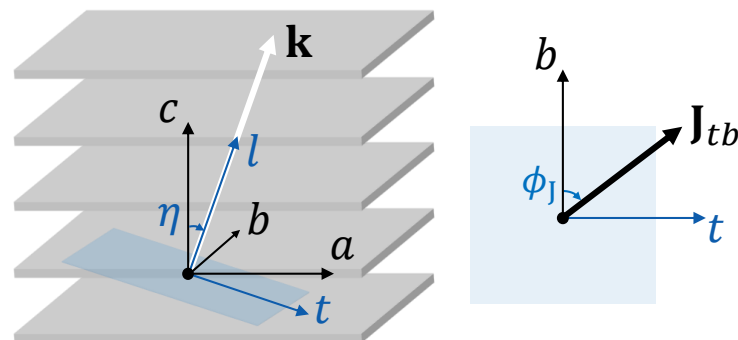
Figure 1. Sketch of the notation used in the manuscript to define the reference frames. The crystalline orientation defines the frame (a, b, c), and the direction of the momentum defines (t, b, l). The angles η and ϕ_J are also represented. The *tb*-plane is highlighted in blue.

Because of anisotropy, the charge mobility within the planes is much higher than in between stacked layers, and the current **J** in the material is, in general, not parallel to **E**, unless propagation occurs along the principal axes of the crystal (a, b, c). Indeed, in general, one can write the conductivity tensor as follows:

$$\begin{pmatrix} J_a \\ J_b \\ J_c \end{pmatrix} = \begin{pmatrix} \sigma_{ab} & 0 & 0 \\ 0 & \sigma_{ab} & 0 \\ 0 & 0 & \sigma_c \end{pmatrix} \begin{pmatrix} E_a \\ E_b \\ E_c \end{pmatrix}, \tag{1}$$

where σ_{ab} and σ_c are the in-plane and out-of-plane conductivities, respectively. In the following, we simplify the tensorial notation by writing the reference frame where a quantity is considered as its subscript, e.g., Equation (1) reads $\mathbf{J}_{abc} = \hat{\sigma}_{abc}\mathbf{E}_{abc}$. If the

wave propagates perpendicularly to the planes ($\eta = 0$), the electric field oscillates within the SC sheets and one directly extracts σ_{ab} from the measured transmissivity/reflectivity; analogously, with a wave propagating within the planes ($\eta = \pi/2$), one can measure σ_c. However, for a generic value of the propagation angle, the measured conductivity will be a combination of the two quantities. In other words, for **k** at a generic angle of η, the current **J** will develop both longitudinal and transverse components with respect to the momentum.

To see this explicitly, we perform a rotation of angle η around the *b*-axis to move in the reference frame (t, b, l), where l labels the longitudinal components and t labels the transverse component with respect to the momentum in the *ac*-plane, while preserving the second transverse component b. In this frame, Equation (1) transforms into $\mathbf{J}_{tbl} = \hat{\sigma}_{tbl}\mathbf{E}_{tbl}$, where the conductivity tensor now reads as follows:

$$\hat{\sigma}_{tbl} = \begin{pmatrix} \sigma_{ab}\cos^2\eta + \sigma_c\sin^2\eta & 0 & (\sigma_c - \sigma_{ab})\sin\eta\cos\eta \\ 0 & \sigma_{ab} & 0 \\ (\sigma_c - \sigma_{ab})\sin\eta\cos\eta & 0 & \sigma_{ab}\sin^2\eta + \sigma_c\cos^2\eta \end{pmatrix}. \tag{2}$$

Notice that the components J_t and J_l are coupled to both E_t and E_l, as one expects in an anisotropic crystal, whereas the transverse J_b component only couples to E_b. As we will detail below, what one determines experimentally is an effective conductivity defined as the ratio between the transverse current and the transverse electric field. According to Ampere's law, $\frac{4\pi}{c}\mathbf{J} + \frac{\varepsilon_\infty}{c}\frac{\partial\mathbf{E}}{\partial t} = 0$, where c is the light velocity and ε_∞ is the background dielectric constant, ensuring that the current in the longitudinal direction is compensated by the displacement current. We then derive the relation $4\pi J_l - i\omega\varepsilon_\infty E_l = 0$, which can be used to eliminate the longitudinal component and write a system that only takes the transverse components t and b into consideration, $\mathbf{J}_{tb} = \hat{\sigma}_{tb}\mathbf{E}_{tb}$. The transverse conductivity tensor reads as follows:

$$\hat{\sigma}_{tb} = \begin{pmatrix} \sigma_t & 0 \\ 0 & \sigma_{ab} \end{pmatrix}, \tag{3}$$

where

$$\sigma_t(\omega, \eta) = \frac{-\frac{i\omega\varepsilon_\infty}{4\pi}\left(\sigma_{ab}\cos^2\eta + \sigma_c\sin^2\eta\right) + \sigma_{ab}\sigma_c}{-\frac{i\omega\varepsilon_\infty}{4\pi} + \sigma_{ab}\sin^2\eta + \sigma_c\cos^2\eta}. \tag{4}$$

For an electric field polarized along t ($E_b = 0$), Equation (4) immediately gives the conductivity we are looking for, $\sigma_t = J_t/E_t$. This expression was first derived in Ref. [34]; its real part displays a peak with the central frequency that moves with η. To show it explicitly, we replace $\sigma_{ab} = \frac{i\omega}{4\pi}\frac{\varepsilon_\infty\omega_{ab}^2}{(\omega+i0^+)^2}$ and $\sigma_c = \frac{i\omega}{4\pi}\frac{\varepsilon_\infty\omega_c^2}{(\omega+i0^+)^2}$, where ω_{ab} and ω_c are the in-plane and out-of-plane plasma frequencies, respectively: one then immediately sees that the real part of $\sigma_t(\omega, \eta)$ peaks at a frequency of $\omega_l(\eta)$, which reads as follows:

$$\omega_l^2(\eta) = \omega_{ab}^2\sin^2\eta + \omega_c^2\cos^2\eta. \tag{5}$$

As we will discuss below, ω_l does *not* define a plasma mode of the system; this can be immediately understood within a classical approach, by writing explicitly the dielectric function corresponding to the conductivity (4). By using $\sigma_{ab} = -\frac{i\omega}{4\pi}(\varepsilon_{ab} - \varepsilon_\infty)$ and $\sigma_c = -\frac{i\omega}{4\pi}(\varepsilon_c - \varepsilon_\infty)$, we can write the in-plane ε_{ab} and out-of-plane ε_c dielectric functions of the SC system as follows:

$$\varepsilon_{ab}(\omega) = \varepsilon_\infty\left(1 - \frac{\omega_{ab}^2}{(\omega+i0^+)^2}\right), \tag{6}$$

and

$$\varepsilon_c(\omega) = \varepsilon_\infty\left(1 - \frac{\omega_c^2}{(\omega+i0^+)^2}\right). \tag{7}$$

Thus, Equation (4) can be recast as $\sigma_t = -\frac{i\omega}{4\pi}(\varepsilon_t - \varepsilon_\infty)$, where

$$\varepsilon_t(\omega, \eta) = \varepsilon_\infty \frac{\left((\omega + i0^+)^2 - \omega_{ab}^2\right)\left((\omega + i0^+)^2 - \omega_c^2\right)}{(\omega + i0^+)^2\left((\omega + i0^+)^2 - \omega_l^2(\eta)\right)}. \tag{8}$$

In Equation (8), the frequency $\omega_l(\eta)$ in Equation (5) appears as a divergence of the dielectric function, while the plasma frequencies in the long-wavelength limit appear as zeros of the dielectric function. This already proves that the scale ω_l does not identify a true plasma mode. However, as we will demonstrate below, it turns out that ω_l provides a good approximation for the *finite-momentum* longitudinal plasmon of the layered system *at large momenta*, i.e., in the momentum regions where retardation effects are no longer relevant. As a consequence, the present results show that the optical absorptive peak in the tilted geometry, which appears as a linear response in the long-wavelength limit, can be used to indirectly access the plasma-wave dispersions at large momenta. Notice that, in principle, Equation (4) is valid, in general, for any collective mode in an anisotropic uniaxial system, provided that the corresponding expressions of $\sigma_{ab}(\omega)$ and $\sigma_c(\omega)$ are used.

Even though these considerations solve the problem of defining a transverse conductivity at tilted angles for an electric field polarized along t, two main issues remain. The first one regards the connection between the frequency of the peak (5) and the real plasma modes of the anisotropic superconductor. The second point is to link these results to the measured quantity in an experiment with a generic polarization of the electric field. The first matter will be discussed in the next section using a quantum formalism based on the description of electromagnetic modes via the SC phase degree of freedom. The second issue will be the subject of the last section, where we will explicitly study the Fresnel problem for transmission/reflection through a sample grown at a tilt. Furthermore, we will discuss the dependence of the measurement on the polarization ϕ of the external incident's electric field.

3.2. Linear Response of Generalized Plasma Modes

3.2.1. Effective Action Description of Plasma Modes

To gain more physical insight into the results of the previous section, we will take advantage of the description of the plasma modes in the SC state obtained via the phase degrees of freedom. Indeed, as recently discussed in Refs. [18,19], this approach is both powerful and elegant in describing the interplay between longitudinal and transverse plasma waves in a layered superconductor, which leads to generalized plasma modes with mixed character at low momenta. Here, we summarize the main ingredients of the derivation, referring the reader to Refs. [18,19] and the references therein for a detailed derivation of the layered phase-only model.

Below the critical temperature T_c, the neighboring SC planes interact with a Josephson-like coupling [3,12,23,38–41] that is much weaker than the in-plane phase stiffness. Following the notation set above, we denote the in-plane superfluid stiffness by D_{ab} and the out-of-plane one by D_c, and we write the Gaussian action for the phase fluctuations θ as follows [42–44]:

$$S_G[\theta] = \frac{1}{8}\sum_q \left[\kappa_0\Omega_m^2 + D_{ab}k_{ab}^2 + D_c k_c^2\right]|\theta(q)|^2, \tag{9}$$

where $q = (i\Omega_m, \mathbf{k})$ is the imaginary-time 4-momentum, with $\Omega_m = 2\pi mT$ representing the bosonic Matsubara frequencies. Here, $k_{ab} = \sqrt{k_a^2 + k_b^2}$ and k_c are the in-plane and out-of-plane momenta, respectively, and κ_0 is the compressibility. In the following, we will denote by $|\mathbf{k}|^2 = k_{ab}^2 + k_c^2$. We introduce the electromagnetic field $\mathbf{A}$ by performing in Equation (9) the minimal coupling substitution $i\mathbf{k}\theta \to i\mathbf{k}\theta + 2e\mathbf{A}/c$, where $-e$ is the charge of the electron, and we will also add the action of the free electromagnetic field [1], as follows:

$$S_{\text{e.m.}}[\mathbf{A}] = \frac{1}{8\pi c^2} \sum_q \left[\varepsilon_\infty \Omega_m^2 |\mathbf{A}(q)|^2 + c^2 |\mathbf{k} \times \mathbf{A}(q)|^2 \right], \tag{10}$$

Both the minimal coupling substitution and Equation (10) are written in the Weyl gauge where the scalar potential is zero. We then recast the coupling between the phase fluctuations and the electromagnetic field by performing the substitution:

$$\boldsymbol{\psi}(q) = i\mathbf{k}\theta(q) + \frac{2e}{c}\mathbf{A}(q). \tag{11}$$

These gauge-invariant fields provide a full description of the plasma modes once the phase fluctuations are integrated out [18,19]. To provide simple analytical expressions, in the following, we consider the limit for infinite compressibility. This is a good approximation in single-layer cuprates, as the effects of finite compressibility on the properties of the generalized plasma modes are negligible at small momenta [18]. Interestingly, these effects are actually crucial when studying the optical absorptive peak of bilayer superconductors [4–9,13,15], whose central frequency is significantly influenced by the compressibility [45,46] due to the capacitive coupling between planes surviving at vanishing momentum [19]. In the basis $\boldsymbol{\psi}_{abc} = \begin{pmatrix} \psi_a & \psi_b & \psi_c \end{pmatrix}^T$, the action of the systems after the integration of θ reads as follows:

$$S[\boldsymbol{\psi}_{abc}] = \frac{1}{32\pi e^2} \sum_q \boldsymbol{\psi}_{abc}^T(-q) \begin{pmatrix} \Omega_m^2 \varepsilon_{ab} + c^2 k_c^2 & 0 & -c^2 k_a k_c \\ 0 & \Omega_m^2 \varepsilon_{ab} + c^2 |\mathbf{k}|^2 & 0 \\ -c^2 k_a k_c & 0 & \Omega_m^2 \varepsilon_c + c^2 k_a^2 \end{pmatrix} \boldsymbol{\psi}_{abc}(q), \tag{12}$$

where we set the in-plane momentum along the a-direction ($k_b = 0$) without loss of generality, such that ψ_b is decoupled, in full analogy with the case of Equation (2). In the action we have defined, using the Matsubara formalism, the in-plane dielectric function is as follows:

$$\varepsilon_{ab}(i\Omega_m) = \varepsilon_\infty \left(1 + \frac{\omega_{ab}^2}{\Omega_m^2} \right), \tag{13}$$

and the out-of-plane dielectric function is as follows:

$$\varepsilon_c(i\Omega_m) = \varepsilon_\infty \left(1 + \frac{\omega_c^2}{\Omega_m^2} \right), \tag{14}$$

where the plasma frequencies are linked to the in-plane and out-of-plane superfluid stiffness, $\omega_{ab}^2 = 4\pi e^2 D_{ab}/\varepsilon_\infty$ and $\omega_c^2 = 4\pi e^2 D_c/\varepsilon_\infty$, respectively. Indeed, these go back to Equations (6) and (7) once the analytic continuation $i\Omega_m \to \omega + i0^+$ is performed. Notice that the dielectric tensor is diagonal in the basis $\boldsymbol{\psi}_{abc}$, as (a, b, c) is the reference frame of the principal axes of the crystal. By their definition in Equation (11), the gauge-invariant fields are formally proportional to the currents; thus, within the effective-action framework, we can apply the same procedure used above in the classical approach, i.e., a change of the reference frame to describe a transverse dielectric tensor. We, thus, perform a rotation around the b-axis that combines the ψ_a and ψ_c components into transverse ψ_t and longitudinal ψ_l components with respect to the momentum $\mathbf{k}$. The matrix that performs the change of basis $\boldsymbol{\psi}_{abc} \to \boldsymbol{\psi}_{tbl} = \begin{pmatrix} \psi_t & \psi_b & \psi_l \end{pmatrix}^T$ reads as follows:

$$U = \begin{pmatrix} k_c/|\mathbf{k}| & 0 & k_a/|\mathbf{k}| \\ 0 & 1 & 0 \\ -k_a/|\mathbf{k}| & 0 & k_c/|\mathbf{k}| \end{pmatrix}, \tag{15}$$

and Equation (12) transforms in this basis as follows:

$$S[\boldsymbol{\psi}_{tbl}] = \frac{1}{32\pi e^2} \sum_q \boldsymbol{\psi}_{tbl}^T(-q) \mathcal{D}_{tbl}^{-1} \boldsymbol{\psi}_{tbl}(q), \tag{16}$$

where the matrix of the coefficients reads

$$\mathcal{D}_{tbl}^{-1} = \begin{pmatrix} \Omega_m^2 (\varepsilon_{ab} k_c^2 + \varepsilon_c k_a^2)/|\mathbf{k}|^2 + c^2 |\mathbf{k}|^2 & 0 & \Omega_m^2 (\varepsilon_c - \varepsilon_{ab}) k_a k_c /|\mathbf{k}|^2 \\ 0 & \Omega_m^2 \varepsilon_{ab} + c^2 |\mathbf{k}|^2 & 0 \\ \Omega_m^2 (\varepsilon_c - \varepsilon_{ab}) k_a k_c /|\mathbf{k}|^2 & 0 & \Omega_m^2 (\varepsilon_{ab} k_a^2 + \varepsilon_c k_c^2)/|\mathbf{k}|^2 \end{pmatrix}. \tag{17}$$

Before moving forward and studying the linear response, we will provide a brief review of the generalized plasma modes that Equation (16) describes. This review will be useful in the following to provide a physical interpretation of the finite-frequency peak in the real part of the conductivity. The action identifies two longitudinal-transverse mixed modes and one decoupled purely transverse mode along the b-direction. The former ones cannot be studied separately, as the anisotropy of layered superconductors is such that the ψ_t and ψ_l components are coupled for the generic directions of the momenta, i.e., the off-diagonal elements of Equation (17) are nonvanishing. On physical grounds, this is a manifestation of retardation effects: as seen in the previous section, at a generic wave vector, the current induced in the system is not parallel to $\mathbf{E}$. This induces a longitudinal electric field in the system in response to a *transverse* perturbation, making longitudinal and transverse responses unavoidably mixed. Since the displacement current scales as $\partial \mathbf{E}/\partial(ct)$, the corrections coming from retardation effects are also named relativistic, as they vanish when $c \to \infty$. The dispersion relations of the two modes obtained from Equation (17) read as follows:

$$\omega_\pm^2(\mathbf{k}) = \frac{1}{2} \left(\omega_{ab}^2 + \omega_c^2 + \frac{c^2}{\varepsilon_\infty} |\mathbf{k}|^2 \pm \sqrt{(\omega_{ab}^2 - \omega_c^2)^2 + \frac{c^4}{\varepsilon_\infty^2} |\mathbf{k}|^4 - 2\frac{c^2}{\varepsilon_\infty}(k_a^2 - k_c^2)(\omega_{ab}^2 - \omega_c^2)} \right), \tag{18}$$

A detailed discussion of the properties of the generalized plasma modes of single-layer anisotropic superconductors can be found in Ref. [18]. Nonetheless, it is important here to stress the main physical outcomes of the present derivation. The generalized dispersions (18) describe two regular functions of the momenta that give $\omega_+(\mathbf{k} \to 0) \to \omega_{ab}$ and $\omega_-(\mathbf{k} \to 0) \to \omega_c$. For generic propagation direction η and for momenta $|\mathbf{k}| \lesssim \bar{k} = \sqrt{\varepsilon_\infty(\omega_{ab}^2 - \omega_c^2)}/c$, these modes have mixed longitudinal/transverse character, with a degree of mixing that is maximum at $\eta = \pi/4$ and vanishes as one moves along the main crystallographic direction ($k_a = 0$ or $k_c = 0$), as one immediately realizes by the structure of the off-diagonal matrix elements of Equation (17), scaling as $k_a k_c$. Explicitly neglecting this coupling, i.e., setting the off-diagonal elements to zero, would result in having the two modes uncoupled, one of which is purely transverse and the other purely longitudinal. In this case, the dispersion relation of the latter, by definition, the plasma mode of the system, can be found by setting to zero the bottom-right element of $\mathcal{D}_{tbl}^{-1}$:

$$\varepsilon_{ab}(\omega) \frac{k_a^2}{|\mathbf{k}|^2} + \varepsilon_c(\omega) \frac{k_c^2}{|\mathbf{k}|^2} = \varepsilon_{ab}(\omega) \sin^2 \eta + \varepsilon_c(\omega) \cos^2 \eta = 0, \tag{19}$$

where we have performed the analytic continuation $i\Omega_m \to \omega + i0^+$ and used $k_c = |\mathbf{k}| \cos \eta$ and $k_a = |\mathbf{k}| \sin \eta$. Using the definitions of the dielectric functions in Equations (13) and (14), the solution of Equation (19) is exactly the frequency, i.e.,

$$\omega_l^2(\mathbf{k}) = \omega_{ab}^2 \frac{k_a^2}{|\mathbf{k}|^2} + \omega_c^2 \frac{k_c^2}{|\mathbf{k}|^2} \equiv \omega_{ab}^2 \sin^2 \eta + \omega_c^2 \cos^2 \eta, \tag{20}$$

as defined in Equation (5). In addition, one can easily see from Equation (18) that in the limit $c \to \infty$, i.e., in the regime where $\bar{k}/|\mathbf{k}| \to 0$, retardation (or relativistic) effects can be neglected; thus, one obtains the following:

$$\omega_-(\mathbf{k}) \to \omega_l(\mathbf{k}), \quad |\mathbf{k}| \gg \bar{k} = \sqrt{\varepsilon_\infty(\omega_{ab}^2 - \omega_c^2)}/c. \tag{21}$$

In other words, the expression $\omega_l(\eta)$ defines the longitudinal plasmon dispersion in a layered superconductor that one obtains by neglecting retardation effects, as one usually does in the standard RPA approach where only Coulomb interactions are included [42–44,47–50]. We also note in passing that the limit of $\omega_l(\mathbf{k})$ for $\mathbf{k} \to 0$ is non-regular as it depends on the direction η of the momentum. As shown above, this is not the case for the real electromagnetic mode ω_-, which is regular at $|\mathbf{k}| = 0$. In Figure 2a, we show $\omega_-(\mathbf{k})$ and $\omega_l(\eta)$ for small values of the propagation angle: as one can see, as $|\mathbf{k}|$ overcomes the $\bar{k}$ scale, ω_- rapidly approaches the ω_l limit and the mode becomes longitudinal. By using realistic values of plasma frequencies in cuprates, one sees that $\bar{k} \sim \mu m^{-1}$. As such, this scale is two orders of magnitude smaller than the momenta usually accessible in RIXS [25–29] or EELS [30–32] experiments, which are not sensitive to the relativistic regime and probe the plasmon dispersion given by Equation (20).
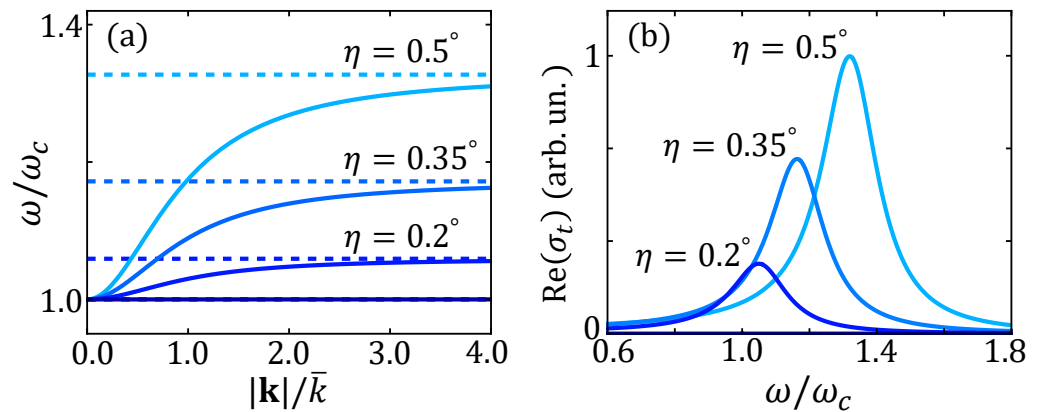
Figure 2. (**a**) Dispersion of the Josephson plasma mode $\omega_-(\mathbf{k})$ (solid lines) and $\omega_l(\eta)$ (dashed lines) for different small propagation angles, having chosen $\omega_{ab}/\omega_c = 100$. (**b**) The real part of the conductivity σ_t in the case of superconducting plasma modes for corresponding values of η of panel (**a**). The conductivity spectra are normalized to the maximum value of the peak at $\eta = 0.5°$. The phenomenological damping parameter is taken as $\gamma = 0.1\omega_c$.

3.2.2. Interpretation of the Conductivity Peak Of Plasmons

From the action in Equation (16), we can perform the integration of ψ_l and work with an action of the transverse components $\boldsymbol{\psi}_{tb} = \begin{pmatrix} \psi_t & \psi_b \end{pmatrix}^T$ only. This procedure is equivalent to using Ampere's law as a condition to eliminate the longitudinal components; see Equation (2) and the discussion below. One is left with an action that reads as follows:

$$S[\boldsymbol{\psi}_{tb}] = \frac{1}{32\pi e^2} \sum_q \boldsymbol{\psi}_{tb}^T(-q) \begin{pmatrix} \Omega_m^2 \varepsilon_t + c^2|\mathbf{k}|^2 & 0 \\ 0 & \Omega_m^2 \varepsilon_{ab} + c^2|\mathbf{k}|^2 \end{pmatrix} \boldsymbol{\psi}_{tb}(q), \qquad (22)$$

where

$$\varepsilon_t(i\Omega_m, \eta) = \frac{\varepsilon_{ab}\varepsilon_c}{\varepsilon_{ab}\sin^2\eta + \varepsilon_c\cos^2\eta}, \qquad (23)$$

is a dielectric function that describes the transverse linear response of the superconductor along the t-axis. Indeed, by making use of the relation $\varepsilon_\alpha = \varepsilon_\infty + 4\pi i\sigma_\alpha/\omega$ between the optical conductivity and the dielectric function along the direction α [51], one recovers σ_t as in Equation (4). Remarkably, the denominator of ε_t can be brought back to the left-hand side of the characteristic Equation (19) for the uncoupled longitudinal mode. Indeed, by using the explicit expressions in Equations (13) and (14) for the in-plane and out-of-plane dielectric functions of plasma modes, and performing the analytic continuation $i\Omega_m \to \omega + i0^+$, one can rewrite Equation (23) as $\varepsilon_t(\omega, \eta) = \varepsilon_\infty(\omega^2 - \omega_{ab}^2)(\omega^2 - \omega_c^2)/[\omega^2(\omega^2 - \omega_l^2(\eta))]$, exactly as in Equation (8) above.

While this result has been formally obtained within Maxwell's classical formalism in the previous section, we can now identify the energy of the peak in the *transverse* conductivity at vanishing momentum as the value of the *longitudinal* plasma mode in the high-momentum regime. This is the same regime usually probed by EELS and RIXS since $\omega_l(\eta)$ is a good approximation of the dispersion of the lower mode $\omega_-(\mathbf{k})$ for $|\mathbf{k}| \gg \bar{k}$; see Equation (21).

The real part of the conductivity σ_t is shown in Figure 2b, where we also introduce a finite damping parameter γ when performing the analytic continuation $i\Omega_m \to \omega + i\gamma$. We emphasize once more that such a peak is not a direct manifestation of the Josephson plasmon of the superconductor [33–36], which, as discussed above, for vanishing momentum is at frequency ω_c for every direction η. Indeed, plasma modes appear as zeroes of the dielectric function and do not lead to finite-frequency peaks in the conductivity. Instead, the absorptive peak at $\omega_l(\eta)$ is a manifestation of the mixing mechanism between in-plane and out-of-plane plasma modes described in the previous section, as the dielectric function in Equation (8) comes directly from the action for the coupled modes in Equation (16). On a more general ground, our derivation clarifies that a signature of a longitudinal nature appears in the transverse response whenever the longitudinal mode is coupled to the transverse one without directly participating in the detection, i.e., the degree of freedom is integrated out.

It is worth mentioning that our derivation is not restricted to electron-doped cuprates, where the peak has already been experimentally reported [33–36], but it is valid for any single-layer superconductor, like the hole-doped LSCO. We also point out that the results could be extended to bilayer superconductors like YBCO, which display two Josephson plasmons at frequencies ω_{c1} and ω_{c2}. Indeed, by using the out-of-plane bilayer dielectric function [5] $\varepsilon_c = \varepsilon_\infty(\omega^2 - \omega_{c1}^2)(\omega^2 - \omega_{c2}^2)/[\omega^2(\omega^2 - \omega_T^2)]$, with $\omega_T^2 = \omega_{c1}^2 d_2 + \omega_{c2}^2 d_1$ and $d_{1,2}$ representing the intra- and inter-bilayer spacings, one can predict two absorptive peaks in the conductivity. These peaks are centered at the high-momentum values of the dispersions of the Josephson modes [19]. The high-energy peak follows the same trend as the peak in single-layer superconductors, moving with η from ω_{c1} to ω_{ab}. The low-energy one quickly moves from ω_{c2} to ω_T even for small values of η and does not disappear for $\eta = \pi/2$ [4–9,13,15]. As mentioned above, finite compressibility corrections are crucial for optical measurements in bilayer superconductors [45,46], and they must be taken into account to correctly fit the experimental data [19].

3.3. Fresnel Equations at Normal Incidence on a Tilted-Grown Sample

To link the results obtained in the previous sections to experiments, we must consider the measured quantity, which is the electric field transmitted or reflected through the sample relative to the incident wave, and relate it to the conductivity σ_t. Moreover, one might argue that due to the fact that the system is anisotropic, both angles η and ϕ_J that define the current propagation within the material differ, respectively, from η_{in}, the angle between the incident momentum of the external wave and the normal to the planes, and ϕ, the angle between the *b*-axis and the electric field that describes its polarization. To this aim, we must write the Fresnel conditions at the boundaries of the sample. In this section, we analyze the configuration where a THz pulse is at normal incidence on a thin-film layered superconductor, grown with tilted planes at a small angle η [33–36], and we show that in this case, the theoretical results can be easily related to experiments; see Appendix A.

Following the notation set above, we define the reference frame (t, b, l) such that the *tb*-plane corresponds to the interface and the *l*-axis is perpendicular to it, see Figure 3a. At normal incidence, $\eta_{in} = \eta$ immediately, as the momentum of the wave does not change direction when crossing the interface. Within the material, the *b*-polarized and *t*-polarized electric fields are decoupled and travel with different values of the wave vector; see Equation (16) and the discussion below. In particular, from Equation (17), the equations of motion read $|\mathbf{k}|^2 = \omega^2 \varepsilon_{ab}/c^2$ for the former and $|\mathbf{k}|^2 = \omega^2 \varepsilon_t/c^2$ for the latter [22], with ε_t defined in Equation (23). We then impose the continuity of the tangential components of

the electric fields, E_t and E_b, and of the magnetic fields, B_t and B_b, at interfaces $l = 0$ and $l = d$, with d denoting the sample thickness. By solving the system set by these conditions, one finds the transmission and reflection coefficients for the t and b components of the field in the thin-film configuration, which read as follows:

$$T_t = \frac{\mathcal{T}_t \mathcal{T}_t' e^{in_t \omega d/c}}{1 - \mathcal{R}_t^2 e^{2in_t \omega d/c}}, \tag{24}$$

$$R_t = \frac{\mathcal{R}_t(1 - e^{2in_t \omega d/c})}{1 - \mathcal{R}_t^2 e^{2in_t \omega d/c}}, \tag{25}$$

$$T_b = \frac{\mathcal{T}_b \mathcal{T}_b' e^{in_b \omega d/c}}{1 - \mathcal{R}_b^2 e^{2in_b \omega d/c}}, \tag{26}$$

$$R_b = \frac{\mathcal{R}_b(1 - e^{2in_b \omega d/c})}{1 - \mathcal{R}_b^2 e^{2in_b \omega d/c}}, \tag{27}$$

where $n_\alpha = \sqrt{\varepsilon_\alpha}$ is the refractive index along the direction α, $\mathcal{T}_\alpha = 2/(1 + n_\alpha)$ is the transmission coefficient going from the vacuum to the material, $\mathcal{T}_\alpha' = 2n_\alpha/(1 + n_\alpha)$ is—analogously—the transmission coefficient from the sample to the vacuum, and $\mathcal{R}_\alpha^2 = 1 - \mathcal{T}_\alpha \mathcal{T}_\alpha'$ accounts for the Fabry–Perot interference within the thin film. The ratios T_t/T_b and R_t/R_b carry the information on the rotation of the polarization of the transmitted or reflected wave. By definition of the dielectric function ε_t in Equation (23), one has that $\varepsilon_t \simeq \varepsilon_{ab}$ under the assumption of the small tilt angle of the planes. Then $n_t \simeq n_b$ and the ratios are approximately 1: one can, thus, conclude that the polarization of the transmitted or reflected wave does not differ significantly from one of the incident waves in the experiment. With the same reasoning, $\sigma_t \simeq \sigma_{ab}$, so that the transverse current is approximately parallel to the field; see Equation (3). We can conclude that $\phi \simeq \phi_J$.
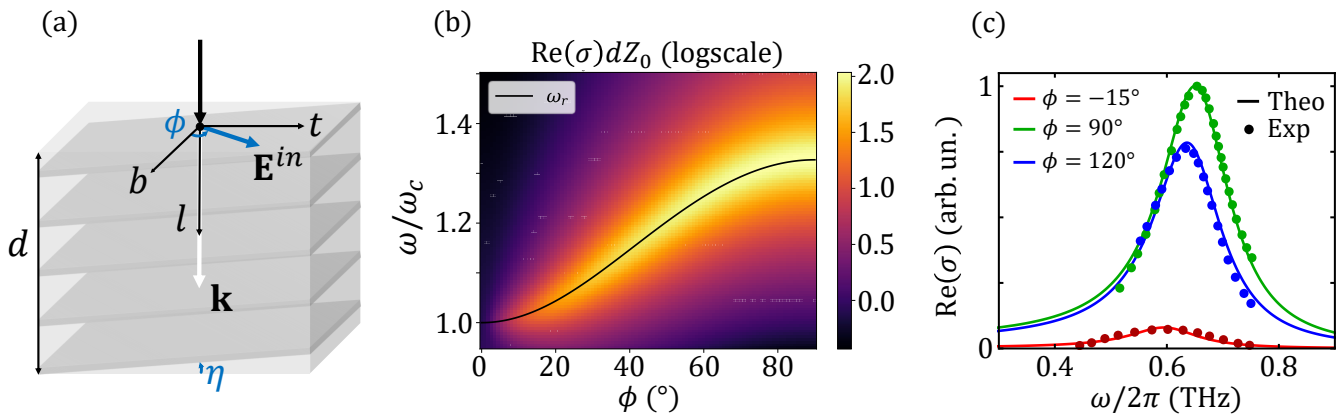
Figure 3. (**a**) Sketch of the experimental configuration with a THz wave at normal incidence on a tilted-grown sample of thickness d. The reference frame (t, b, l) for this configuration is also shown to highlight the direction of the external electric field $\mathbf{E}^{in}$ that defines the polarization angle ϕ. (**b**) The real part of the measured conductivity as a function of frequency and the polarization angle as in Equation (30). The solid black line corresponds to $\omega_r(\eta, \phi)$ as in Equation (32). In this plot, $\eta = 0.25°$, $d = 0.150 \ \mu m$, $\omega_{ab}/\omega_c = 100$ and $\gamma = 0.1\omega_c$. (**c**) The fit of experimental data from Ref. [36] with $\sigma(\omega, \eta, \phi)$ for different polarization angles. Fitting parameters are extracted at once from the following measurements: $\omega_{ab}/2\pi = 60$ THz, $\omega_c/2\pi = 0.6$ THz, $\eta = 0.26°$, $\gamma = 0.075$ THz.

In an experiment, the measured quantity (see Appendix A) is either the transmissivity, as follows:

$$T = T_b \cos^2 \phi + T_t \sin^2 \phi, \tag{28}$$

or, analogously, the reflectivity, as follows:

$$R = R_b \cos^2 \phi + R_t \sin^2 \phi. \tag{29}$$

From these quantities, one can define the measured transverse conductivity. Indeed, under the assumption of film-thickness d, which is much smaller than the wavelength of the radiation inside the material and its penetration depth, one finds the following [36]:

$$\sigma(\omega, \eta, \phi) = \frac{2}{Z_0 d} \left(\frac{1}{T} - 1 \right), \tag{30}$$

where $Z_0 = 4\pi/c$ is the impedance of free space. This proportionality establishes the link between the measured quantity and the theoretical conductivity we are looking for. Moreover, regarding cuprates, one can numerically estimate $T \ll 1$ in Equation (28), and then approximate $\sigma \propto 1/T$. Since $\sigma_{ab} \propto 1/T_b$ and $\sigma_t \propto 1/T_t$, from (28), one can express the measured transverse conductivity as follows:

$$\sigma(\omega, \eta, \phi) \simeq \frac{\sigma_{ab}\sigma_t}{\sigma_{ab} \sin^2 \phi + \sigma_t \cos^2 \phi}. \tag{31}$$

With σ_t from Equation (4) and using the expressions of σ_{ab} and σ_c for the superconductor, one finds that the real part of the conductivity has a peak at a resonance frequency $\omega_r(\eta, \phi)$ that depends on both η and ϕ:

$$\omega_r^2(\eta, \phi) = \frac{\omega_{ab}^2 \sin^2 \eta \sin^2 \phi + \omega_c^2 (1 - \sin^2 \eta \sin^2 \phi)}{1 - \sin^2 \eta \cos^2 \phi + \left(\frac{\omega_c}{\omega_{ab}} \right)^2 \sin^2 \eta \cos^2 \phi}. \tag{32}$$

In Figure 3b, we show the real part of Equation (30) as a function of the external polarization angle and we compare the peak in the measured conductivity with Equation (32). Indeed, the approximated expression (31) provides an excellent description of the experimental data in Refs. [33–36], and the frequency Equation (32) establishes a link between the peak of the experimental conductivity and the plasma frequencies ω_{ab} and ω_c, which can then be extracted as fitting parameters given the angles η and ϕ. In Figure 3c, we fit experimental data from Ref. [36] to provide an estimate of the in-plane and out-of-plane plasma frequencies of the overdoped $La_{1.87}Ce_{0.13}CuO_4$ ($T_c = 21$ K) at 5 K. We clarify that the experimental fit is not meant to draw any conclusion on the symmetry of the superconducting order parameter, which is still debated in the context of electron-doped cuprates[36,52]. Equation (9), which is our starting point, can be derived from a microscopic model, which admits a modulation of the superconducting gap[19]. At the level of Equation (9), the gap symmetry influences the temperature dependence of the superfluid stiffnesses D_{ab} and D_c, which are primarily controlled by quasiparticle excitations, while barely affecting the charge compressibility κ_0. In addition, the gap symmetry can impact the quasiparticle damping of the plasmon, controlling the phenomenological broadening γ, even though other mechanisms can determine its value independently of the gap symmetry. However, once the proper gap symmetry is embedded in the plasma frequencies ω_{ab} and ω_c, the structure of the modes in Equation (18) is general.

So far, it has been empirically observed in Ref. [33] that the data could be well fitted using an effective conductivity $\sigma_t(\omega, \eta_{\text{eff}})$ having the same functional form as Equation Equation (4), but with an effective tilt angle $\eta_{\text{eff}} = \eta \sin \phi$. This result follows from Equation (31) in the case of a small angle η between the momentum and the c-axis of the crystal, which is indeed the configuration of Ref. [33]. In this case, the frequency of the peak in Equation (32) can be approximated as follows:

$$\omega_r^2(\eta, \phi) \simeq \omega_{ab}^2 \sin^2 \eta_{\text{eff}} + \omega_c^2 \cos^2 \eta_{\text{eff}} = \omega_l^2(\eta_{\text{eff}}), \tag{33}$$

where again $\eta_{\text{eff}} = \eta \sin \phi$.

At first, one might consider the configuration where the THz pulse is incident at a small angle on a c-axis grown sample. However, computing the Fresnel conditions in this

scenario results in featureless transmissivity and reflectivity, and no peak appears in the real part of the conductivity (see Appendix A for details)

4. Discussion

In this manuscript, we studied the optical absorption in layered superconductors within a tilted geometry, where light propagates inside the sample by forming a small angle with the stacking direction. We demonstrated that such a geometry enables observation with optics—a fundamentally zero-momentum probe—of a direct signature of the plasmon dispersion at momenta of the order of a fraction of the Brillouin zone, which is typically probed by RIXS or EELS. The basic physical mechanism behind this observation is the intrinsic mixing between transverse and longitudinal electromagnetic modes in a layered material due to the anisotropy between the in-plane and out-of-plane response. Such mixing, which is absent when light propagates along the main crystallographic axes, leads to the emergence of an absorption peak in the transverse optical conductivity in tilted geometry. Interestingly, we can analytically show that the peak frequency moves as a function of the tilting angle according to the functional law that the physical longitudinal plasmon displays at momenta larger than the scale where transverse/longitudinal mixing is relevant. In cuprates, where the SC c-axis plasmon is weakly affected by Landau damping due to the opening of a large spectral gap below T_c, the peak is well-defined at a small tilting angle, and it has indeed been observed in several electron-doped cuprates [33–36]. Here, we argue that the same effect can be seen in any layered sample, provided that the appropriate Fresnel geometry is implemented. In addition, we provide an analytical expression for the peak frequency as a function of both tilting angle and light polarization, which can be used to derive from a single set of measurements the relevant scales for plasma excitations in these systems. It is worth stressing that in recent years, after charged plasmons were detected for the first time with high-resolution RIXS [25–29] and EELS [30–32] experiments, an intense discussion emerged on the nature of charge fluctuations in these correlated materials [31,32]. The all-optical measurement proposed here is in principle a bulk probe; it is not affected by the lack of sensitivity at small momenta associated with plasmon measurements via charge-detecting probes and allows for precise control over the momentum value, which can be problematic, e.g., with EELS [32]. As a consequence, the experimental verification of this idea could provide an additional tool to explore charge fluctuations in cuprates and their possible interplay with other collective modes of the systems.

Author Contributions: Conceptualization, L.B.; methodology, N.S., J.F., C.C. and L.B.; writing—original draft preparation, N.S.; writing—review and editing, N.S., J.F., C.C. and L.B.; supervision, L.B.; funding acquisition, L.B. All authors have read and agreed to the published version of the manuscript.

Data Availability Statement: Data are contained within the article.

Conflicts of Interest: The authors declare no conflicts of interest. The funders had no role in the design of the study; in the collection, analyses, or interpretation of data; in the writing of the manuscript; or in the decision to publish the results.
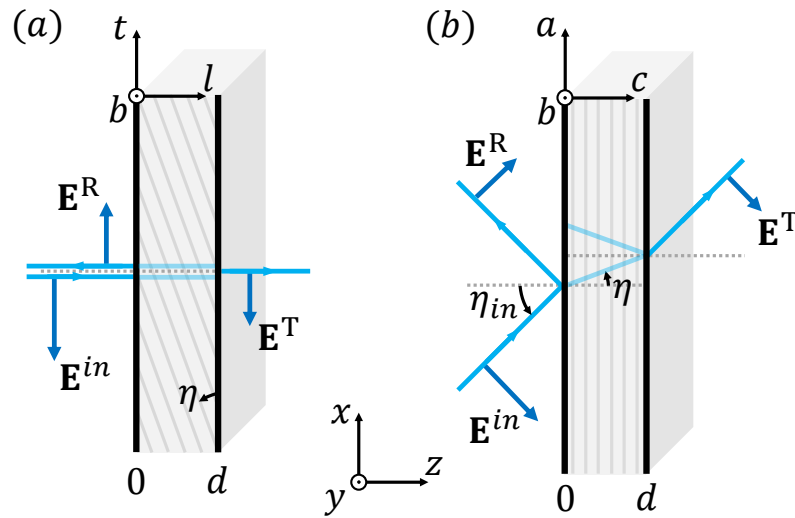
Appendix A

In this appendix, we calculate the transmitted electric field for two experimental configurations, where the electromagnetic wave travels at a finite angle with respect to the stacking direction of the planes, using standard Fresnel-like boundary conditions applied to a uniaxial film. Let us consider a transmission experiment on a superconductor placed

in the region $0 < z < d$, as in Figure A1. The electric field satisfies Maxwell's equations, as follows:

$$\begin{cases} \nabla^2 \mathbf{E} - \frac{1}{c^2}\frac{\partial^2 \mathbf{E}}{\partial t^2} = 0 & z < 0,\ z > d \\ \nabla^2 \mathbf{E} - \nabla(\nabla \cdot \mathbf{E}) - \frac{1}{c^2}\frac{\partial^2 (\hat{\varepsilon}\mathbf{E})}{\partial t^2} = 0 & 0 < z < d \end{cases}, \tag{A1}$$

where $\hat{\varepsilon}$ is the dielectric tensor of the uniaxial material. By expanding the electric field on a basis of plane waves, Equation (A1) becomes a linear system for the Cartesian Fourier components of the electric field, as follows:

$$\begin{cases} (|\mathbf{k}|^2 - \omega^2/c^2)\delta_{\alpha\beta} E_\beta = 0 & z < 0,\ z > d \\ (|\mathbf{k}|^2\delta_{\alpha\beta} - k_\alpha k_\beta - \omega^2\varepsilon_{\alpha\beta}/c^2)E_\beta = 0 & 0 < z < d \end{cases}. \tag{A2}$$

Figure A1. Sketch of the two possible experimental configurations discussed in this appendix. In both cases, the reference frame (x, y, z) is defined such that xy is the vacuum-sample interface and xz is the plane of incidence. For graphical purposes, only TM-polarized waves are depicted. (**a**) Geometry of the configuration where the THz pulse incident at normal incidence on a thin-film crystal is grown with layers tilted at an angle η with respect to the vacuum-sample interface, as in Section 3.3. In this case, the (x, y, z) reference frame corresponds to the (t, b, l) frame introduced in the main text. (**b**) The geometry of the configuration where the incident field is at oblique incidence with angle η_{in} on a thin-film sample with planes parallel to the interface. In this case, the (x, y, z) reference frame corresponds to the crystallographic (a, b, c) frame.

A propagating solution is allowed whenever the determinant of this system is zero. For the experimental configuration in Figure A1a, where the frame (x, y, z) corresponds to (t, b, l), as in Section 3.3, the incoming momentum is along the z (or l) direction. In this geometry, the dielectric tensor is defined as follows (see Equations (2) and (17)):

$$\hat{\varepsilon} = \begin{pmatrix} \varepsilon_{ab}\cos^2\eta + \varepsilon_c\sin^2\eta & 0 & (\varepsilon_{ab} - \varepsilon_c)\cos\eta\sin\eta \\ 0 & \varepsilon_{ab} & 0 \\ (\varepsilon_{ab} - \varepsilon_c)\cos\eta\sin\eta & 0 & \varepsilon_{ab}\sin^2\eta + \varepsilon_c\cos^2\eta \end{pmatrix}. \tag{A3}$$

From Equation (A2), one can see that the subspace associated with E_y is decoupled from the ones associated with E_x and E_z. As a consequence, one can see immediately that y-polarized electric fields in the material propagate with wave vector $|\mathbf{k}|^2 = \omega^2\varepsilon_{ab}/c^2$, while x- and z-polarized electric fields propagate with wave vector $|\mathbf{k}|^2 = \omega^2\varepsilon_t/c^2$, where

$$\varepsilon_t = \frac{\varepsilon_{ab}\varepsilon_c}{\varepsilon_{ab}\sin^2\eta + \varepsilon_c\cos^2\eta}, \tag{A4}$$

as in Equation (23) in the main text. Conversely, for the experimental configuration in Figure A1b, where the frame (x, y, z) corresponds to the crystallographic frame (a, b, c), the dielectric tensor is diagonal $\hat{\varepsilon}_{\alpha\beta} = \varepsilon_\alpha \delta_{\alpha\beta}$ (see Equations (1) and (12)). As the wave vector belongs to the xz-plane, in this case, the equation for E_y is decoupled from the other two components. In both cases, one can then solve the system separately for the transmission of the $y-$ and the mixed $xz-$ polarized components of $\mathbf{E}$. In the following, we will refer to the former component as the transverse electric (TE) field and to the latter as the transverse magnetic (TM) field, as one would commonly do in the oblique incidence configuration where the plane of incidence is xz. Notice that the transmitted wave $\mathbf{E}^T$ is generically polarized along a direction ϕ' that differs from the polarization ϕ of the incident wave $\mathbf{E}^{in}$, although the experiment is still set to measure the outgoing ϕ-polarized wave $\mathbf{E}^{T'}$. Assuming that the TE and TM transmission coefficients are known, such that $E_{TE,TM}^T = T_{TE,TM} E_{TE,TM}^{in}$ (see Figure A2 for the notation), one finds the measured transmitted field polarized along ϕ as

$$
\begin{aligned}
E^{T'} &= E^T \cos(\phi' - \phi) \\
&= E^T \cos\phi' \cos\phi + E^T \sin\phi' \sin\phi \\
&= T_{TE} E_{TE}^{in} \cos\phi + T_{TM} E_{TM}^{in} \sin\phi \\
&= (T_{TE} \cos^2\phi + T_{TM} \sin^2\phi) E^{in} \equiv T E^{in}.
\end{aligned} \tag{A5}
$$

Analogously, one can express the reflected field in a similar way. For the configuration discussed in Section 3.3, see Figure A1a, the TE and TM components stand for the b and t components, respectively, and one obtains Equation (28) from the main text. We now explicitly compute the transmission coefficients T_{TE} and T_{TM} for the two configurations separately.
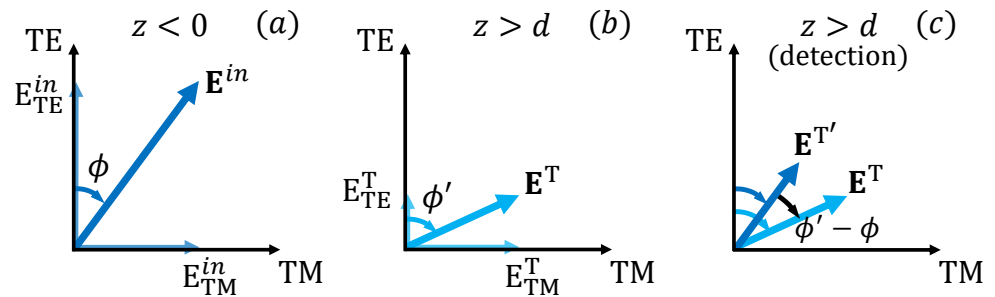
Figure A2. (a) Incoming electric field $\mathbf{E}^{in}$ at a generic polarization angle ϕ with respect to the TE axis (corresponding to the y-axis and the crystallographic b-axis in both configurations of Figure A1). (b) The transmitted electric field $\mathbf{E}^T$ is found using the appropriate set of boundary conditions. The transmitted field still lies in the TM-TE plane due to the conservation of the parallel component of the incident momentum, but $\mathbf{E}^T$ is generically polarized with angle $\phi' \neq \phi$. (c) Comparison between the directions of the transmitted field $\mathbf{E}^T$ and the projected field $\mathbf{E}^{T'}$ along the incoming polarization, which is the measured quantity in a transmission experiment.

For the first configuration (Figure A1a), $T_{TE} \equiv T_b$ and $T_{TM} \equiv T_t$; thus, the TE and TM components propagate with different refractive indices, $n_b = \sqrt{\varepsilon_{ab}}$ and $n_t = \sqrt{\varepsilon_t}$, respectively. Imposing the continuity of the tangential components of the electric $\mathbf{E}$ and magnetic $\mathbf{B}$ fields, one recovers the usual expression for transmission at normal incidence on a slab, namely the following:

$$
T_\alpha = \frac{\mathcal{T}_\alpha \mathcal{T}'_\alpha e^{in_\alpha \omega d/c}}{1 - \mathcal{R}_\alpha^2 e^{2in_\alpha \omega d/c}}, \tag{A6}
$$

where $\mathcal{T}_\alpha = 2/(n_\alpha + 1)$ is the transmission coefficient from vacuum $n = 1$ to a medium with refractive index n_α, and $\mathcal{T}'_\alpha = 2n_\alpha/(n_\alpha + 1)$ is analogously the transmission coefficient from the medium to the vacuum. The denominator accounts for the Fabry–Perot interference inside the slab of thickness d, with $\mathcal{R}^2_\alpha = 1 - \mathcal{T}_\alpha \mathcal{T}'_\alpha$. Equation (A6) can also be expressed as follows:

$$\mathrm{T}_\alpha = \frac{2n_\alpha}{2n_\alpha \cos \zeta_\alpha - i(n^2_\alpha + 1)\sin \zeta_\alpha}, \tag{A7}$$

where $\zeta_\alpha = n_\alpha \omega d/c$. Given the approximation $d \ll |n_\alpha|\omega/c$, meaning that the thickness of the film is much smaller than both the wavelength of the radiation inside the material $\lambda = \mathrm{Re}(n_\alpha)\omega/c$ and the skin depth $\delta = \mathrm{Im}(n_\alpha)\omega/c$, one can approximate to the first order in ζ_α

$$\frac{1}{\mathrm{T}_\alpha} \approx 1 - i\frac{n^2_\alpha + 1}{2n_\alpha}\zeta_\alpha = 1 - i\frac{(n^2_\alpha + 1)\omega d}{2c}. \tag{A8}$$

Using the relation between the refractive index and conductivity $\sigma_\alpha = \frac{\omega}{4\pi i}(n^2_\alpha - 1)$, one can rewrite Equation (A8) as follows:

$$\frac{1}{\mathrm{T}_\alpha} = 1 + \frac{4\pi d\sigma_\alpha}{2c} - i\frac{2\omega d}{c} \approx 1 + \frac{4\pi d\sigma_\alpha}{2c}, \tag{A9}$$

where, again, we consider $\omega d/c \ll 1$. Consequently, one finds the following:

$$\sigma_\alpha = \frac{2}{Z_0 d}\left(\frac{1}{\mathrm{T}_\alpha} - 1\right), \tag{A10}$$

where $Z_0 = 4\pi/c$. This relation between the conductivity and the transmissivity is valid along both the b and t directions. On the other hand, one can imagine extracting an experimental conductivity from the experimental transmissivity T as in Equation (A5) by applying the same relation, see, e.g., Ref. [36], where Equation (30) is used.

In the second configuration (Figure A1b), the interface is parallel to the ab-plane of the crystal, and one needs to solve a wider set of continuity conditions. Indeed, one must impose the continuity of the tangential components of the electric **E** and magnetic **B** fields as with the previous configuration; additionally, the continuity of the normal component of the displacement field **D** must be maintained [53,54]. To understand how the transmission occurs in this case, let us first recall the results expected for an isotropic film, where the propagation of the electromagnetic wave inside the sample is defined by a unique refractive index n. In this case, one easily finds that $\mathrm{T}^{(\mathrm{iso})} \equiv \mathrm{E}^{\mathrm{T}'}/\mathrm{E}^{in}$ reads as follows:

$$\mathrm{T}^{(\mathrm{iso})}(\eta_{in}, n) = \frac{\mathcal{T}\mathcal{T}' e^{in\omega d \cos \eta/c}}{1 - \mathcal{R}^2 e^{2in\omega d \cos \eta/c}}, \tag{A11}$$

where η is the propagation angle inside the material, see Figure A1b, while η_{in} is the external angle of incidence. Here, we define $\mathcal{T} = 2\cos \eta_{in}/(n\cos \eta_{in} + \cos \eta)$ as the transmission coefficient from the vacuum to the medium, and analogously, $\mathcal{T}' = 2n\cos \eta/(n\cos \eta_{in} + \cos \eta)$ as the transmission coefficient from the medium to the vacuum. The denominator of Equation (A11) accounts for the Fabry–Perot interference inside the slab of thickness d, with $\mathcal{R}^2 = 1 - \mathcal{T}\mathcal{T}'$. In Equation (A11), we explicitly state the dependence of the transmissivity T on the incident angle and the refractive index n only. Indeed, the propagation angle inside the sample is automatically defined by these two quantities thanks to Snell's law, which states that $\sin \eta = \sin \eta_{in}/n$ (notice that in the isotropic case, one has to define η with respect to the normal to the interface as there are no planes, but we retain the notation to emphasize the analogy between the two cases. However, in the uniaxial case depicted in Figure A1b, Snell's relation is not valid, since due to the anisotropy of the refractive indices, components k_{ab} and k_c of the momentum are rescaled differently. This makes the transmission coefficient a function of η_{in}, n_b, and n_c. More specifically, for the TM wave, one

finds that T_{TM} has an expression analogous to Equation (A11), provided that one replaces $n \rightarrow n_b = \sqrt{\varepsilon_{ab}}$ and $\sin \eta \rightarrow \sin \eta_{in}/n_c = \sin \eta_{in}/\sqrt{\varepsilon_c}$:

$$T_{TM}(\eta_{in}, n_b, n_c) = \frac{\mathcal{T}\mathcal{T}' e^{in_b \omega d \cos \eta/c}}{1 - \mathcal{R}^2 e^{2in_b \omega d \cos \eta/c}}, \tag{A12}$$

with $\mathcal{T}$ and $\mathcal{T}'$ retaining the same functional dependence on η, η_{in} as before. In this situation, the argument of the complex exponential in Equation (A12) reads as follows:

$$\zeta = n_b \frac{\omega d}{c} \cos \eta = n_b \frac{\omega d}{c} \sqrt{1 - \frac{\sin^2 \eta_{in}}{n_c^2}}. \tag{A13}$$

One can observe that for THz frequencies around the Josephson plasma frequency $\omega \sim \omega_c$, the divergence in the square root when $\eta_{in} \neq 0$ is weakened by the residual quasiparticle damping, γ, so that we obtain $\zeta \ll 1$. Then, evaluating $1/T_{TM}$ from (A12) at small ζ, one has the following:

$$\frac{1}{T_{TM}} \approx 1 - i \frac{\omega d}{2c} \frac{\varepsilon_{ab} \cos^2 \eta_{in} + 1 - \sin^2 \eta_{in}/\varepsilon_c}{\cos \eta_{in}}. \tag{A14}$$

Similar reasonings can be made for the TE component, which is expressed as in Equation (A12), provided that $\sin \eta \rightarrow \sin \eta_{in}/n_b = \sin \eta_{in}/\sqrt{\varepsilon_{ab}}$. Also, in this case, one can approximate the transmission coefficient along this direction as follows:

$$\frac{1}{T_{TE}} \approx 1 - i \frac{\omega d}{2c} \frac{\varepsilon_{ab} \cos^2 \eta_{in} + 1 - \sin^2 \eta_{in}/\varepsilon_{ab}}{\cos \eta_{in}}. \tag{A15}$$

Even though Equations (A14) and (A15) still depend on a combination of ε_{ab} and ε_c, these structures do not lead to the pole observed in the transverse dielectric function ε_t, as opposed to Equation (A8) obtained in the first configuration. In the end, by explicit numerical computation with realistic parameter values for cuprates of the transmissivity T_{TM} and T_{TE} in Equation (A12), with the corresponding definitions of η, we can verify that the corresponding conductivities, expressed as in Equation (A10), are featureless, and no finite-frequency peaks are observed.

References

1. Nagaosa, N.; Heusler, S. *Quantum Field Theory in Condensed Matter Physics*; Texts and Monographs in Physics; Springer: New York, NY, USA, 1999.
2. Anderson, P.W. Random-Phase Approximation in the Theory of Superconductivity. *Phys. Rev.* **1958**, *112*, 1900–1916. [CrossRef]
3. Keimer, B.; Kivelson, S.A.; Norman, M.R.; Uchida, S.; Zaanen, J. From quantum matter to high-temperature superconductivity in copper oxides. *Nature* **2015**, *518*, 179–186. [CrossRef] [PubMed]
4. Homes, C.C.; Timusk, T.; Liang, R.; Bonn, D.A.; Hardy, W.N. Optical conductivity of c axis oriented YBa$_2$Cu$_3$O$_{6.70}$: Evidence for a pseudogap. *Phys. Rev. Lett.* **1993**, *71*, 1645–1648. [CrossRef] [PubMed]
5. van der Marel, D.; Tsvetkov, A. Transverse optical plasmons in layered superconductors. *Czechoslov. J. Phys.* **1996**, *46*, 3165. [CrossRef]
6. Shibata, H.; Yamada, T. Double Josephson Plasma Resonance in T^* Phase SmLa$_{1-x}$Sr$_x$CuO$_{4-ffi}$. *Phys. Rev. Lett.* **1998**, *81*, 3519–3522. [CrossRef]
7. Grüninger, M.; van der Marel, D.; Tsvetkov, A.A.; Erb, A. Observation of Out-of-Phase Bilayer Plasmons in YBa$_2$Cu$_3$O$_{7-ffi}$. *Phys. Rev. Lett.* **2000**, *84*, 1575–1578. [CrossRef] [PubMed]
8. van der Marel, D.; Tsvetkov, A.A. Transverse-optical Josephson plasmons: Equations of motion. *Phys. Rev. B* **2001**, *64*, 024530. [CrossRef]
9. Dubroka, A.; Rössle, M.; Kim, K.W.; Malik, V.K.; Munzar, D.; Basov, D.N.; Schafgans, A.A.; Moon, S.J.; Lin, C.T.; Haug, D.; et al. Evidence of a Precursor Superconducting Phase at Temperatures as High as 180 K in RBa$_2$Cu$_3$O$_{7-\delta}$ ($R = $ Y, Gd, Eu) Superconducting Crystals from Infrared Spectroscopy. *Phys. Rev. Lett.* **2011**, *106*, 047006. [CrossRef] [PubMed]
10. Stinson, H.T.; Wu, J.S.; Jiang, B.Y.; Fei, Z.; Rodin, A.S.; Chapler, B.C.; McLeod, A.S.; Castro Neto, A.; Lee, Y.S.; Fogler, M.M.; et al. Infrared nanospectroscopy and imaging of collective superfluid excitations in anisotropic superconductors. *Phys. Rev. B* **2014**, *90*, 014502. [CrossRef]
11. Lu, Q.; Bollinger, A.T.; He, X.; Sundling, R.; Bozovic, I.; Gozar, A. Surface Josephson plasma waves in a high-temperature superconductor. *npj Quantum Mater.* **2020**, *5*, 69. [CrossRef]

12. Savel'ev, S.; Yampol'skii, V.A.; Rakhmanov, A.L.; Nori, F. Terahertz Josephson plasma waves in layered superconductors: spectrum, generation, nonlinear and quantum phenomena. *Rep. Prog. Phys.* **2010**, *73*, 026501. [CrossRef]

13. Hu, H.; Kaiser, S.; Nicoletti, D.; Hunt, C.R.; Gierz, I.; Hoffmann, M.C.; Le Tacon, M.; Loew, T.; Keimer, B.; Cavalleri, A. Optically enhanced coherent transport in YBa2Cu3O6.5 by ultrafast redistribution of interlayer coupling. *Nat. Mater.* **2014**, *13*, 705–711. [CrossRef] [PubMed]

14. Rajasekaran, S.; Okamoto, J.; Mathey, L.; Fechner, M.; Thampy, V.; Gu, G.D.; Cavalleri, A. Probing optically silent superfluid stripes in cuprates. *Science* **2018**, *359*, 575–579. [CrossRef] [PubMed]

15. Zhang, S.J.; Wang, Z.X.; Xiang, H.; Yao, X.; Liu, Q.M.; Shi, L.Y.; Lin, T.; Dong, T.; Wu, D.; Wang, N.L. Photoinduced Nonequilibrium Response in Underdoped $YBa_2Cu_3O_{6+x}$ Probed by Time-Resolved Terahertz Spectroscopy. *Phys. Rev. X* **2020**, *10*, 011056. [CrossRef]

16. Katsumi, K.; Nishida, M.; Kaiser, S.; Miyasaka, S.; Tajima, S.; Shimano, R. Near-infrared light-induced superconducting-like state in underdoped $YBa_2Cu_3O_y$ studied by *c*-axis terahertz third-harmonic generation. *Phys. Rev. B* **2023**, *107*, 214506. [CrossRef]

17. Kaj, K.; Cremin, K.A.; Hammock, I.; Schalch, J.; Basov, D.N.; Averitt, R.D. Terahertz third harmonic generation in *c*-axis $La_{1.85}Sr_{0.15}CuO_4$. *Phys. Rev. B* **2023**, *107*, L140504. [CrossRef]

18. Gabriele, F.; Castellani, C.; Benfatto, L. Generalized plasma waves in layered superconductors: A unified approach. *Phys. Rev. Res.* **2022**, *4*, 023112. [CrossRef]

19. Sellati, N.; Gabriele, F.; Castellani, C.; Benfatto, L. Generalized Josephson plasmons in bilayer superconductors. *Phys. Rev. B* **2023**, *108*, 014503. [CrossRef]

20. Gabriele, F.; Senese, R.; Castellani, C.; Benfatto, L. Charge-density response in layered metals: Retardation effects, generalized plasma waves, and their spectroscopic signatures. *Phys. Rev. B* **2024**, *109*, 045137. [CrossRef]

21. Bulaevskii, L.N.; Zamora, M.; Baeriswyl, D.; Beck, H.; Clem, J.R. Time-dependent equations for phase differences and a collective mode in Josephson-coupled layered superconductors. *Phys. Rev. B* **1994**, *50*, 12831–12834. [CrossRef]

22. Helm, C.; Bulaevskii, L.N. Optical properties of layered superconductors near the Josephson plasma resonance. *Phys. Rev. B* **2002**, *66*, 094514. [CrossRef]

23. Laplace, Y.; Cavalleri, A. Josephson plasmonics in layered superconductors. *Adv. Phys. X* **2016**, *1*, 387–411. [CrossRef]

24. Salvador, A.G.; Dolgirev, P.E.; Michael, M.H.; Liu, A.; Pavicevic, D.; Fechner, M.; Cavalleri, A.; Demler, E. Principles of 2D terahertz spectroscopy of collective excitations: The case of Josephson plasmons in layered superconductors. *arXiv* **2024**, arXiv:2401.05503.

25. Hepting, M.; Chaix, L.; Huang, E.W.; Fumagalli, R.; Peng, Y.Y.; Moritz, B.; Kummer, K.; Brookes, N.B.; Lee, W.C.; Hashimoto, M.; et al. Three-dimensional collective charge excitations in electron-doped copper oxide superconductors. *Nature* **2018**, *563*, 374–378. [CrossRef] [PubMed]

26. Lin, J.; Yuan, J.; Jin, K.; Yin, Z.; Li, G.; Zhou, K.J.; Lu, X.; Dantz, M.; Schmitt, T.; Ding, H.; et al. Doping evolution of the charge excitations and electron correlations in electron-doped superconducting La2-xCexCuO4. *npj Quantum Mater.* **2020**, *5*, 4. [CrossRef]

27. Nag, A.; Zhu, M.; Bejas, M.; Li, J.; Robarts, H.C.; Yamase, H.; Petsch, A.N.; Song, D.; Eisaki, H.; Walters, A.C.; et al. Detection of Acoustic Plasmons in Hole-Doped Lanthanum and Bismuth Cuprate Superconductors Using Resonant Inelastic X-ray Scattering. *Phys. Rev. Lett.* **2020**, *125*, 257002. [CrossRef]

28. Singh, A.; Huang, H.Y.; Lane, C.; Li, J.H.; Okamoto, J.; Komiya, S.; Markiewicz, R.S.; Bansil, A.; Lee, T.K.; Fujimori, A.; et al. Acoustic plasmons and conducting carriers in hole-doped cuprate superconductors. *Phys. Rev. B* **2022**, *105*, 235105. [CrossRef]

29. Bejas, M.; Zimmermann, V.; Betto, D.; Boyko, T.D.; Green, R.J.; Loew, T.; Brookes, N.B.; Cristiani, G.; Logvenov, G.; Minola, M.; et al. Plasmon dispersion in bilayer cuprate superconductors. *arXiv* **2023**, arXiv:2311.01413.

30. Mitrano, M.; Husain, A.A.; Vig, S.; Kogar, A.; Rak, M.S.; Rubeck, S.I.; Schmalian, J.; Uchoa, B.; Schneeloch, J.; Zhong, R.; et al. Anomalous density fluctuations in a strange metal. *Proc. Natl. Acad. Sci. USA* **2018**, *115*, 5392–5396. [CrossRef]

31. Husain, A.A.; Mitrano, M.; Rak, M.S.; Rubeck, S.; Uchoa, B.; March, K.; Dwyer, C.; Schneeloch, J.; Zhong, R.; Gu, G.D.; et al. Crossover of Charge Fluctuations across the Strange Metal Phase Diagram. *Phys. Rev. X* **2019**, *9*, 041062. [CrossRef]

32. Thornton, S.J.; Liarte, D.B.; Abbamonte, P.; Sethna, J.P.; Chowdhury, D. Jamming and unusual charge density fluctuations of strange metals. *Nat. Commun.* **2023**, *14*, 3919. [CrossRef] [PubMed]

33. Pimenov, A.; Pronin, A.V.; Loidl, A.; Kampf, A.P.; Krasnosvobodtsev, S.I.; Nozdrin, V.S. Submillimeter spectroscopy of tilted $Nd_{1.85}Ce_{0.15}CuO_{4-\text{ffi}}$ films: Observation of a mixed ac-plane excitation. *Appl. Phys. Lett.* **2000**, *77*, 429–431. [CrossRef]

34. Pimenov, A.; Pronin, A.V.; Loidl, A.; Michelucci, U.; Kampf, A.P.; Krasnosvobodtsev, S.I.; Nozdrin, V.S.; Rainer, D. Anisotropic conductivity of $Nd_{1.85}Ce_{0.15}CuO_{4-\text{ffi}}$ films at submillimeter wavelengths. *Phys. Rev. B* **2000**, *62*, 9822–9826. [CrossRef]

35. Pimenov, A.; Pronin, A.V.; Loidl, A.; Tsukada, A.; Naito, M. Peak in the far-infrared conductivity of strongly anisotropic cuprates. *Phys. Rev. B* **2002**, *66*, 212508. [CrossRef]

36. Tagay, Z.; Mahmood, F.; Legros, A.; Sarkar, T.; Greene, R.L.; Armitage, N.P. BCS *d*-wave behavior in the terahertz electrodynamic response of electron-doped cuprate superconductors. *Phys. Rev. B* **2021**, *104*, 064501. [CrossRef]

37. van der Marel, D.; Kim, J.H.; Feenstra, B.J.; Wittlin, A. Comment on "Evidence for a-b-plane coupling to longitudinal c-axis phonon in high T_c superconductors". *Phys. Rev. Lett.* **1993**, *71*, 2676–2676. [CrossRef] [PubMed]

38. Shibauchi, T.; Kitano, H.; Uchinokura, K.; Maeda, A.; Kimura, T.; Kishio, K. Anisotropic penetration depth in $La_{2-x}Sr_xCuO_4$. *Phys. Rev. Lett.* **1994**, *72*, 2263–2266. [CrossRef] [PubMed]

39. Panagopoulos, C.; Cooper, J.R.; Peacock, G.B.; Gameson, I.; Edwards, P.P.; Schmidbauer, W.; Hodby, J.W. Anisotropic magnetic penetration depth of grain-aligned $HgBa_2Ca_2Cu_3O_{8+\text{ffi}}$. *Phys. Rev. B* **1996**, *53*, R2999–R3002. [CrossRef] [PubMed]

40. Hosseini, A.; Broun, D.M.; Sheehy, D.E.; Davis, T.P.; Franz, M.; Hardy, W.N.; Liang, R.; Bonn, D.A. Survival of the *d*-Wave Superconducting State near the Edge of Antiferromagnetism in the Cuprate Phase Diagram. *Phys. Rev. Lett.* **2004**, *93*, 107003. [CrossRef]

41. Fazio, R.; van der Zant, H. Quantum phase transitions and vortex dynamics in superconducting networks. *Phys. Rep.* **2001**, *355*, 235–334. [CrossRef]

42. Paramekanti, A.; Randeria, M.; Ramakrishnan, T.V.; Mandal, S.S. Effective actions and phase fluctuations in d-wave superconductors. *Phys. Rev. B* **2000**, *62*, 6786–6799. [CrossRef]

43. Benfatto, L.; Caprara, S.; Castellani, C.; Paramekanti, A.; Randeria, M. Phase fluctuations, dissipation, and superfluid stiffness in d-wave superconductors. *Phys. Rev. B* **2001**, *63*, 174513. [CrossRef]

44. Sun, Z.; Fogler, M.M.; Basov, D.N.; Millis, A.J. Collective modes and terahertz near-field response of superconductors. *Phys. Rev. Res.* **2020**, *2*, 023413. [CrossRef]

45. Pimenov, A.; Loidl, A.; Dulić, D.; van der Marel, D.; Sutjahja, I.M.; Menovsky, A.A. Magnetic Field Dependence of the Transverse Plasmon in $SmLa_{0.8}Sr_{0.2}CuO_{4-\delta}$. *Phys. Rev. Lett.* **2001**, *87*, 177003. [CrossRef] [PubMed]

46. Dulić, D.; Pimenov, A.; van der Marel, D.; Broun, D.M.; Kamal, S.; Hardy, W.N.; Tsvetkov, A.A.; Sutjaha, I.M.; Liang, R.; Menovsky, A.A.; et al. Observation of the Transverse Optical Plasmon in $SmLa_{0.8}Sr_{0.2}CuO_{4-ffi}$. *Phys. Rev. Lett.* **2001**, *86*, 4144–4147. [CrossRef] [PubMed]

47. Benfatto, L.; Toschi, A.; Caprara, S. Low-energy phase-only action in a superconductor: A comparison with the XY model. *Phys. Rev. B* **2004**, *69*, 184510. [CrossRef]

48. Fertig, H.A.; Das Sarma, S. Collective modes in layered superconductors. *Phys. Rev. Lett.* **1990**, *65*, 1482–1485. [CrossRef] [PubMed]

49. Fertig, H.A.; Das Sarma, S. Collective excitations and mode coupling in layered superconductors. *Phys. Rev. B* **1991**, *44*, 4480–4494. [CrossRef] [PubMed]

50. Hwang, E.H.; Das Sarma, S. Collective modes and their coupling to pair-breaking excitations in layered d-wave superconductors. *Phys. Rev. B* **1995**, *52*, R7010–R7013. [CrossRef]

51. Melnyk, A.R.; Harrison, M.J. Theory of Optical Excitation of Plasmons in Metals. *Phys. Rev. B* **1970**, *2*, 835–850. [CrossRef]

52. Fan, J.Q.; Yu, X.Q.; Cheng, F.J.; Wang, H.; Wang, R.; Ma, X.; Hu, X.P.; Zhang, D.; Ma, X.C.; Xue, Q.K.; et al. Direct observation of nodeless superconductivity and phonon modes in electron-doped copper oxide $Sr_{1-x}Nd_xCuO_2$. *Natl. Sci. Rev.* **2021**, *9*, nwab225. [CrossRef] [PubMed]

53. Mosteller, L.P.; Wooten, F. Optical Properties and Reflectance of Uniaxial Absorbing Crystals. *J. Opt. Soc. Am.* **1968**, *58*, 511–518. [CrossRef]

54. Schützmann, J.; Somal, H.S.; Tsvetkov, A.A.; van der Marel, D.; Koops, G.E.J.; Koleshnikov, N.; Ren, Z.F.; Wang, J.H.; Brück, E.; Menovsky, A.A. Experimental test of the interlayer pairing models for high-T_c superconductivity using grazing-incidence infrared reflectometry. *Phys. Rev. B* **1997**, *55*, 11118–11121. [CrossRef]